Physics of Fluids ARTICLE pubs.aip.org/aip/pof

Hydrodynamic modes in nano-channels

Cite as: Phys. Fluids **37**, 012021 (2025); doi: 10.1063/5.0232561
Submitted: 8 August 2024 · Accepted: 11 December 2024 ·
Published Online: 13 January 2025

Solvej Knudsen,[1,2] B. D. Todd,[2] and J. S. Hansen[1,a)]

AFFILIATIONS

[1]"Glass and Time," IMFUFA, Department of Science and Environment, Roskilde University, Postbox 260, DK-4000 Roskilde, Denmark
[2]Department of Mathematics, School of Science, Computing and Engineering Technologies, Swinburne University of Technology, Victoria 3122, Australia

[a)]Author to whom correspondence should be addressed: jschmidt@ruc.dk

ABSTRACT

This paper investigates the local hydrodynamics of a dense fluid confined in nanoscale slit-pores with different heights. Using non-equilibrium molecular dynamics simulations of the fluid system, we induce a steady-state sinusoidal velocity profile across the channel having a characteristic wavelength, thus, probing the fluid response to a specific Fourier mode. As expected, for sufficiently large channel heights and wavelengths there is an excellent agreement between the hydrodynamic predictions and simulation data. As the wavelength decreases to around 5 molecular diameters, the classical hydrodynamics fails to predict the steady-state velocity profile; we attribute this to the non-local nature of the fluid response and the presence of density gradients in the wall–fluid interfacial region. Using generalized hydrodynamics and the Fourier spectrum of the density profile, we derive the strain rate amplitude and shear pressure corrections due to these two effects. The local relaxation from the steady-state to the zero flow situation is tracked for different channel heights and wavelengths. The relaxation is in general visco-elastic in the wall–fluid region, and we argue that this phenomenon is the mechanism behind the "enhanced viscosity" used in the literature. We also report a surprising dynamics for the fluid located between the wall–fluid region and bulk region, which cannot be explained by classical hydrodynamics; here, an initial exponential relaxation abruptly transitions into a linear relaxation. The work highlights the many different physical mechanisms present in nano-confined fluids, and that the fluid response is in general position and wavelength dependent.

I. INTRODUCTION

Understanding hydrodynamics on the nanoscale has been a very active research field for decades[1–5] and supports the technological advancement of fabricating and utilizing increasingly smaller lab-on-a-chip devices.[6] It is well known that classical hydrodynamic theory can, in fact, be applied on surprisingly small length scales: Koplik *et al.*[7] and Travis *et al.*[8] showed that for a fluid flow in a slit-pore of a height of just ten particle diameters, the hydrodynamic prediction agrees very well with molecular dynamics simulation results. More recently, Hansen[9] investigated hydrodynamic correlation functions in equilibrium, again using molecular dynamics, concluding that the theory is valid down to around 10 nm for different model liquid systems.

The classical predictions will eventually break down as mechanisms relevant on extreme small scales emerge. This includes coupling between the fluid linear and angular momenta,[10] coupling between polarization and thermal gradient,[11] non-local response calling for generalized linear constitutive relations,[12] and velocity slip boundary conditions.[13,14] It is important to note that experimental data with sufficiently high resolution are often not obtainable and many investigations are based on comparison between theoretical predictions and molecular simulation data, i.e., the latter is considered as an ideal numerical experiment.

Fluid flows in nanoscale tubes and channels are inherently complicated to model, particularly since the fluid can form structures in the wall–fluid interfacial region.[3,15] This structuring can have a characteristic length that is on the same order of magnitude as the channel itself and potentially affects the local transport properties.[16] A lot of work has been devoted to simulate and model these extreme confined fluid systems, see, e.g., Refs. 7 and 17–20; however, there are still unexplored phenomena. For example, it is known that the visco-elastic properties of the fluid are position dependent,[21] but no direct comparison with theoretical predictions or a study of the wavelength dependency has been carried out, to our knowledge.

In this study, we perform a series of direct non-equilibrium molecular dynamics simulations (NEMD), where we employ a spatial sinusoidal external driving force to a simple dense fluid confined between two parallel walls. This allows us to investigate the system response to a specific wavelength, here also denoted Fourier mode.

Therefore, the resulting local steady-state velocity is a function of two characteristic length scales: the force wavelength and channel height. Removing the driving force, we can also follow the local relaxation dynamics, again for the two characteristic length scales just mentioned. The second purpose is to compare the *classical* hydrodynamic theory against the simulation results: We solve the momentum balance equation for the system using two standard constitutive relations: Newton's law of viscosity and Maxwell's visco-elastic model. The comparison tests the classical theory and, moreover, enables us to resolve different local dynamics characterizing the hydrodynamics in nano-scale confinement and analyze the mechanisms that lead to the failure of classical hydrodynamics on these extreme small scales.

II. HYDRODYNAMICS

The system is a fluid confined between two semi-infinite parallel walls. The direction of confinement is the z-direction, see Fig. 1, and the walls lie in the (x, y)-plane. For times $t \leq 0$, the fluid features a sinusoidal steady flow in the x-direction. This is generated by an external driving force given by

$$F_{\text{ext}} = \rho A \sin(k_n z), \tag{1}$$

where ρ is the system density, A the acceleration amplitude, $k_n = 2\pi n/h$ the force wave vector, $n \in \mathbb{N}_+$ is the wave number, and h the channel height. In the theoretical treatment, it is assumed that the acceleration amplitude is sufficiently small such that only the nth Fourier mode in the velocity field is excited. Another way to generate a spatially varying flow is to apply oscillatory shearing in the (x, y)-plane by moving the wall atoms. This resembles an experimental approach; however, it complicates the underlying equations while probing for the same dynamics. For $t \geq 0$, the external force is switched off and we follow the relaxation dynamics.

To derive the hydrodynamic predictions of this scenario, we first derive the steady-state profile which also acts as the initial condition for the relaxation dynamics. The wall–fluid interactions are such that we can assume no-slip Dirichlet boundary conditions. The momentum balance equation for the geometry illustrated in Fig. 1 and for sufficiently low Reynolds numbers is

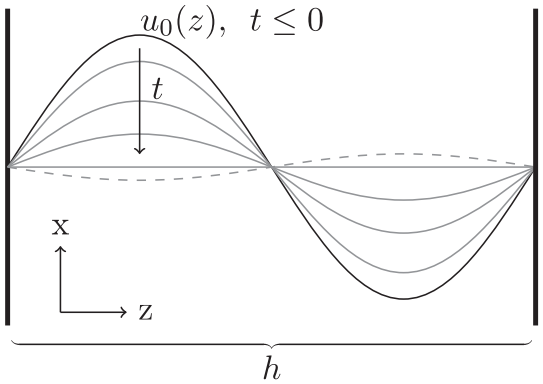

FIG. 1. Schematics of the system under study. For $t < 0$, an external driving force is applied and the velocity profile, $u_0 = u_0(z)$, is a steady-state sinusoidal flow profile. For $t \geq 0$, the external driving force is removed and the velocity profile relaxes toward a zero flow situation. The dashed line illustrates how the relaxation may overshoot under certain conditions.

$$\rho \frac{\partial u}{\partial t} = F_{\text{ext}} - \frac{\partial P_{xz}}{\partial z}, \tag{2}$$

where u is the streaming velocity in the x-direction and P_{xz} the shear xz-component of the pressure tensor. In the steady state, i.e., for $t \leq 0$, the shear pressure is given by Newton's law of viscosity,[22]

$$P_{xz} = -\eta_0 \frac{\partial u}{\partial z}, \tag{3}$$

where η_0 is the shear viscosity. By substitution, we get the equation for the steady-state velocity, $u_0 = u_0(z)$,

$$\frac{\mathrm{d}^2 u_0}{\mathrm{d}z^2} = -\frac{A}{\nu_0} \sin(k_n z), \tag{4}$$

where $\nu_0 = \eta_0/\rho_0$ is the kinematic viscosity under the assumption that the density is constant $\rho = \rho_0$. With the Dirichlet boundary conditions $u_0(0) = u_0(h) = 0$, we get the steady-state solution,

$$u_0(z) = U_n \sin(k_n z), \quad t \leq 0, \tag{5}$$

where the velocity amplitude is related to the wave vector and channel height through

$$U_n = \frac{A}{\nu_0 k_n^2} = \frac{h^2 A}{4n^2 \pi^2 \nu_0}. \tag{6}$$

We can now derive the relaxation dynamics using Eq. (5) as the initial condition.

A. Relaxation of a Newtonian fluid

For the Newtonian relaxation, we substitute Eq. (3) into the momentum balance equation, Eq. (2), and noting that $F_{\text{ext}} = 0$ for $t \geq 0$ we obtain a simple diffusion problem,

$$\frac{\partial u^N}{\partial t} = \nu_0 \frac{\partial^2 u^N}{\partial z^2}. \tag{7}$$

u^N is used to indicate that this is the velocity field obtained from the Newtonian model. With Dirichlet boundaries and the initial condition specified above, this gives the following solution:

$$u^N(z, t) = u_0(z) \exp(-\mu t), \tag{8}$$

where we have introduced the frequency coefficient $\mu = \nu_0 k_n^2$ to ease the reading. The detailed derivation can be found in Appendix A. Through the prefactor U_n, we immediately see that the system relaxation depends on the channel height h and the driving force wavelength.

B. Relaxation of a Maxwellian fluid

To model the visco-elastic relaxation, we apply Maxwell's model,[22,23]

$$\frac{\partial u}{\partial z} = -\frac{1}{\eta_0}\left(1 + \tau_M \frac{\partial}{\partial t}\right) P_{xz}, \tag{9}$$

where τ_M is the Maxwell relaxation time. It is here convenient to formulate the dynamics in Laplace space. To this end, we first note that Eq. (9) in Laplace coordinate, s, is given by

$$\frac{\partial \hat{u}^M}{\partial z} = -\frac{1}{\eta_0}(1+\tau_M s)\hat{P}_{xz}(z,s) + \frac{\tau_M}{\eta_0}P_{xz}(z,0), \tag{10}$$

where the hat-symbol indicates the dynamical variable in Laplace space and superscript M indicates that this is the velocity obtained from Maxwell's model. The initial shear pressure $P_{xz}(z,0)$ is obtained from the steady-state velocity profile u_0, where elastic effects are absent, i.e.,

$$\frac{\partial}{\partial z}P_{xy}(z,0) = \rho_0 A \sin(k_n z). \tag{11}$$

By differentiation of Eq. (10), one then obtains

$$\frac{\partial^2 \hat{u}^M}{\partial z^2} - \frac{s(1+\tau_M s)}{\nu_0}\hat{u}^M = \frac{A}{\eta_0}\frac{\tau_M\mu - (1+\tau_M s)}{\mu}\sin(k_n z). \tag{12}$$

This inhomogeneous differential equation can be solved, see Appendix B for details, giving

$$u^M(z,t) = u_0(z)\exp(-\Gamma t)\Lambda(t). \tag{13}$$

$\Gamma = 1/(2\tau_M)$ is the attenuation coefficient, and Λ is defined as

$$\Lambda(t) = \begin{cases} \dfrac{1-2\tau_M\mu}{\sqrt{1-4\tau_M\mu}}\sinh(\omega_0 t) + \cosh(\omega_0 t), & \tau_M \le 1/(4\mu), \\ \dfrac{1-2\tau_M\mu}{\sqrt{|1-4\tau_M\mu|}}\sin(\omega_0 t) + \cos(\omega_0 t), & \tau_M > 1/(4\mu), \end{cases} \tag{14}$$

where

$$\omega_0 = \sqrt{|1-4\tau_M\mu|}/(2\tau_M) \tag{15}$$

is the characteristic frequency. Notice that there exists a particular Maxwell time, $\tau_M^{\exp} = 1/(4\mu) = 1/(4\nu_0 k_n^2)$, where the temporal part of the solution for u^M changes topology, that is, it goes from a monotonically decreasing function to an oscillatory behavior resembling a damped oscillation. At this time, the relaxation is purely exponential, still it should not be identified as the onset of visco-elastic behavior as this is the case for $\tau_M \neq 0$, but solely as a topological conjugacy value.

Figure 2 shows the temporal factors of u^N (thick full line) and u^M (broken lines) for different Maxwell times. As $\tau_M \to 0$, we get the expected single exponential behavior characterizing a Newtonian fluid. Notice the relatively fast monotonically decreasing relaxation for $0 < \tau_M \le \tau_M^{\exp}$ compared to the purely viscous relaxation.

There are, of course, alternative visco-elastic models, to name a few the Kelvin–Voigt model, Burgers model, and the Maxwell–Weichert element.[22,24] We here test the Maxwell model as this is the standard exemplary and simple model for visco-elastic behavior.

III. SIMULATION RESULTS AND DISCUSSION

A. Molecular dynamics simulations

The dense fluid is composed of simple spherical particles confined between two atomistic walls with a simple cubic lattice structure. All particles have same mass and interact via the cut and shifted Lennard-Jones potential,

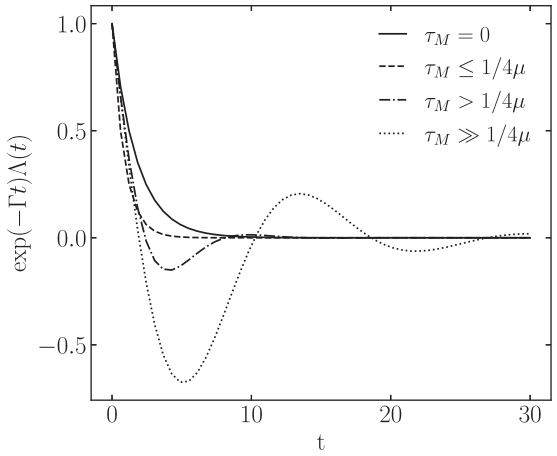

FIG. 2. Temporal dynamics for the Newtonian model, $\tau_M = 0$, (full thick line) and Maxwellian model (punctured lines) for different values of τ_M. The parameter values are $h = 13.6$, $n = 1$, and $\nu_0 = 2.0$ in reduced simulation units, see Sec. III A.

$$U(r) = \begin{cases} 4\epsilon\left[\left(\dfrac{\sigma}{r}\right)^{12} - \left(\dfrac{\sigma}{r}\right)^{6}\right] + U(r_c), & r \le r_c, \\ 0, & r > r_c, \end{cases} \tag{16}$$

where r is the distance between two particles, ϵ is the simulation energy scale, and σ is the characteristic particle diameter defining the simulation length scale. All mechanical quantities can be expressed in terms of σ, ϵ, and particle mass m,[25] and following common practise we will omit writing these units explicitly. In the simulations σ, ϵ, and m are set to unity. All particles interact with same energy and lengths scales, ϵ and σ. The cutoff r_c is set to 2.5 except for the wall–wall particle interactions where $r_c = 2^{1/6}$, that is, the particles are standard Lennard-Jones particles except for the wall–wall interaction, which is given by the Weeks–Chandler–Andersen (WCA) potential. The two walls are each composed of three layers of wall particles in the confining z-direction. The wall particles are bonded to their crystal lattice site using a restoring Hook spring force with a spring constant $\kappa = 500$ for all simulations; the crystal lattice sites have z-coordinates 0.5, 1.5, and 2.5 for the lower (left) wall, and $L_z - 2.5, L_z - 1.5, L_z - 0.5$ for the upper (right) wall. The fluid bulk density is between 0.73 and 0.75 depending on the channel height, and the wall density is $\rho_w = 0.9$, which ensures a non-penetrable wall crystal. The simulation box is rectangular. In the unconfined directions with lengths $L_x = L_y = 20$, while it varies in the confined direction using $L_z = 12$ to $L_z = 50$, see Table I. The particle equations of motion are integrated forward in time using a leap-frog integrator[25] with time step 0.002 or 0.005. Only the wall atoms are thermostated[20] using a heat-bath coupling method[26] with relaxation time of 0.01. The thermostat results in a system temperature $T = 1.1$, and the bulk fluid state corresponds to a liquid state.

First, the steady-state sinusoidal velocity field is obtained by applying the external driving force $\mathbf{F} = [A\sin(k_n z), 0, 0]$ for 10^8 time steps for all simulations, expect for $L = 12$ where 5×10^8 time steps are used. The external field is then turned off and the subsequent relaxation of the velocity profile is monitored. The relaxation is a very fast process and it is subject to large noise-to-signal ratio. Thus,

TABLE I. Table of system details; the confined simulation box length, L_z, the number of fluid particles, N_f, the driving force wave number, n, the magnitude of the driving force, A, the channel height used in the driving force, h_F, the wave vector given by the driving force, k_n, the channel height calculated from the density profile, h_ρ, the half-wavelength, Δz, as estimated from h_ρ.

L_z	N_f	n	A	h_F	k_n	h_ρ	Δz	Sample freq.	Relax. time steps
12	1800	1	2.19×10^{-1}	6	1.05	5.74	2.87	10	2500
20	4200	1	4.03×10^{-2}	14	0.45	13.74	6.87	50	10^4
20	4200	2	1.61×10^{-1}	14	0.90	13.74	∼3.44	10	2500
20	4200	3	2.52×10^{-1}	14	1.35	13.74	∼2.29	10	2500
34	8400	1	1.01×10^{-2}	28	0.22	27.74	13.87	50	16×10^4
50	13 200	1	3.16×10^{-3}	44	0.14	43.73	21.87	50	32×10^4

relaxation data are averaged over at least 1000 independent relaxation runs; for the smallest system, $L_z = 12$, data are averaged over 5000 relaxations.

The channel height is not uniquely defined. In Table I, we list the height given by the (average) non-zero density profile, h_ρ. This value will be smaller than the channel height defined by the distance between the center-of-mass of the two inner most wall layers facing the confined fluid. We use the recommendation from Ref. 5, where it is shown that the former definition is in good agreement with the theoretical predicted height found by Herrero *et al.*[27] and fits simulation data, whereas the latter definition results in a too large flow rate. To drive the flow in the simulations, we use a slightly larger height, h_F, compared to h_ρ to ensure that all fluid particles are accelerated with a local constant amplitude.

The velocity profiles are obtained by dividing the simulation box into 200 bins and calculating the velocity field. In the steady-state, we have[20]

$$u_0(z) = \frac{\left\langle \sum_{i\in\text{bin}} m_i v_{x,i} \right\rangle_t}{\left\langle \sum_{i\in\text{bin}} m_i \right\rangle_t}, \tag{17}$$

where $\langle \ldots \rangle_t$ indicates a sample mean with respect to time. During the relaxation, the number of bins is set to 50 in order to reduce the noise-to-signal ratio and the instantaneous velocity profiles are sampled equivalently according to

$$u(z,t) = \frac{\sum_{i\in\text{bin}} m_i v_{x,i}(t)}{\sum_{i\in\text{bin}} m_i}, \tag{18}$$

and a sample mean is performed after the series of relaxations. The density profile is also obtained using the simple bin method, see Ref. 20.

As input to the hydrodynamic prediction, the fluid shear viscosity is calculated in an equilibrium bulk simulation at the identical state point $(T, \rho_0) = (1.1, 0.75)$ using the standard Green–Kubo integral of the shear pressure;[25] this gives $\eta_0 = 1.61 \pm 0.05$.

B. The steady state

We first address the steady-state profile, u_0. Figure 3 shows the profile for two cases with height $h = h_\rho = 13.74$: In (a), the wave number is $n = 1$ and in (b) $n = 3$. The classical prediction, Eq. (5), where the viscosity is found from independent equilibrium simulation at the bulk state points and no fitting is performed, agrees very well with simulation data for $n = 1$. Notice that the assumption that the kinematic viscosity is constant is valid in this case; this also follows previous studies, see, e.g., Ref. 5. This also means that only one system response mode is excited corresponding to the external force mode. Increasing the driving force magnitude A, we find discrepancy with the prediction at strain rate amplitude of $\dot{\gamma}_0 \approx 0.1$, which defines the upper bound for the Newtonian regime. Also, notice that the no-slip

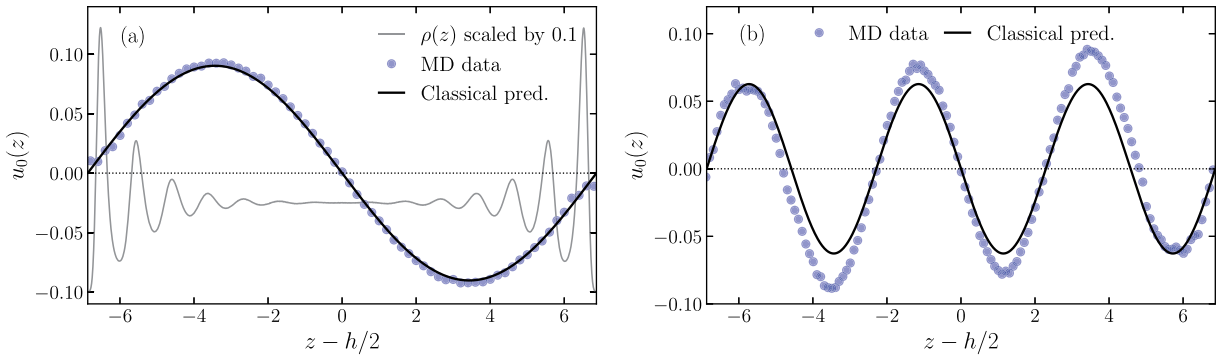

FIG. 3. Steady-state velocity profiles for $n = 1$ (a) and $n = 3$ (b). In both cases, $h = 13.74$. Filled circles are molecular dynamics simulations data and full line the predictions from classical hydrodynamics, Eq. (5). For later comparison, the corresponding density profile for $n = 1$ is also shown (scaled and shifted) and we note that the density profile for $n = 3$ is equivalent. In (a), the strain rate amplitude is 0.020 and in (b) 0.056.

boundary condition is achieved fairly well with this particular system setup.

For shorter wavelengths, $n = 3$, the classical description fails and additional system response modes are excited. The strain rate fulfills $\dot{\gamma}_0 < 0.1$ and we can disregard the discrepancy to be due to non-linear modes. The power spectra for the two velocity profiles are shown in Fig. 4, where the wave vector is normalized with respect to k_n. While only the mode $k = k_n$ is excited when $n = 1$, as discussed above, two additional low intensity (or amplitude) long wavelength modes are excited for $n = 3$. The very low intensity (<1) modes are assigned to the data noise. We will not pursue a more detailed spectral analysis of the velocity profile here but seek to understand the mechanisms behind the additional modes. We highlight that for $n = 3$, we observe that (i) away from the wall–fluid region the velocity amplitude is larger than predicted, (ii) the amplitude features varying magnitude, (iii) in the first half-wave nearest to the wall the flow peak features a small plateau, and (iv) the wavelength is varying in the wall–fluid region.

Todd *et al.*[12] showed that for a system with constant density that undergoes sufficiently small wavelength sinusoidal shear, similar to the one studied here, the local stress (or shear pressure) is reduced. This reduction results in an increased velocity amplitude, when compared to the classical description. The shear pressure reduction is due to the non-local nature of the fluid response, meaning that the stress at a point is not simply given by the strain rate at that particular point, as proposed by the Newtonian constitutive model, but the entire system strain rate distribution.

We will apply this picture as a model for the enhanced velocity amplitude. Assuming that only the main Fourier mode is excited, the strain rate in the bulk region can be written as $\dot{\gamma} = \dot{\gamma}_0/2\ \cos(k_n z)$. The generalized constitutive model for the shear pressure is then

$$P_{xz}(z) = -\eta_0 \dot{\gamma}_0 \int_{-\infty}^{\infty} f(z - z') \cos(k_n z') \mathrm{d}z', \tag{19}$$

where f is the kernel which is an even function around zero and fulfills $\int_{-\infty}^{\infty} f(z) dz = 1$.[5,28] Equation (19) is valid for a bulk system of infinite extent, however, the conclusions from this will be true for the bulk part of the channel as well. Introducing the variable $u = z - z'$, we have

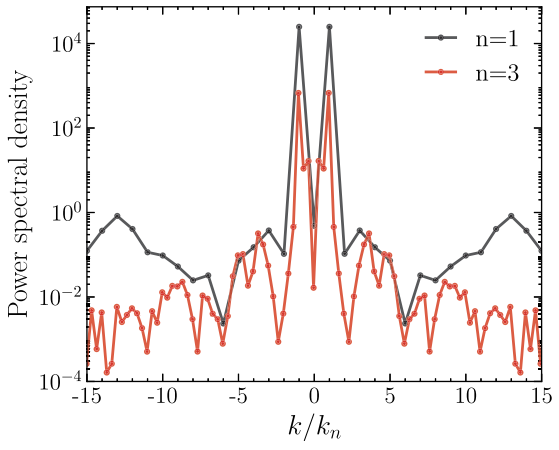

FIG. 4. Normalized power spectra for the two velocity profiles in Fig. 3. Notice that the *y*-axis is a logarithmic scale.

$$P_{xz}(z) = -\eta_0 \dot{\gamma}_0 \int_{-\infty}^{\infty} f(u) \cos(k_n(z - u)) \mathrm{d}u. \tag{20}$$

Taylor expanding the cosine function about the point of interest z, we have

$$\cos(k_n(z - u)) = \cos(k_n z) - k_n \sin(k_n z)(z' - z) - \frac{k_n^2}{2} \cos(k_n)(z\prime - z)^2 + \cdots, \tag{21}$$

and substituting into Eq. (20) and performing the integrals gives

$$P_{xz}(z) = -\eta_0 \dot{\gamma}_0 \left(\cos(k_n z) - k_n^2 f_2 \cos(k_n z) + \cdots\right), \tag{22}$$

where we use

$$\int_{-\infty}^{\infty} u f(u) \mathrm{d}u = 0 \quad \text{and} \quad f_2 = \frac{1}{2} \int_{-\infty}^{\infty} u^2 f(u)\, \mathrm{d}u. \tag{23}$$

Except for the first term, the response goes as even powers of wave vector, and the magnitudes of the terms are determined by the kernel f. As an example, if we choose a Gaussian form for f, say $f(u) = 1/\sqrt{\pi\sigma} \exp(-(u/\sigma)^2)$, see Ref. 5, and let $\sigma = 0.4$ (corresponding to a half width of around particle diameter[12]), we get f_2 approximately equal to 1/20.

The steady-state momentum balance equation is

$$F_{\text{ext}} = \frac{\mathrm{d}P_{xz}}{\mathrm{d}z}, \tag{24}$$

and on substitution of Eqs. (22) and (1) into Eq. (24) we get to second order in k_n,

$$\rho_0 A \sin(k_n z) = \eta_0 \dot{\gamma}_0 k_n (1 - k_n^2 f_2) \sin(k_n z), \tag{25}$$

or by comparing coefficients,

$$\dot{\gamma}_0 = \frac{\rho_0 A}{\eta_0 k_n (1 - k_n^2 f_2)}, \quad 0 < k_n^2 f_2 < 1. \tag{26}$$

Notice that we obtain the classical local result $\dot{\gamma}_0 = \rho_0 A/\eta_0 k_n$ for $k_n \to 0$. Using $f_2 = 1/20$ then for $k_n = 0.45$, Fig. 3(a), we get a strain amplitude increase of approximately 1%, and for $k_n = 1.35$, Fig. 3(b), approximately 10%. This rough estimate is in good agreement with the NEMD data.

We conjecture that points (ii)-(iv) are due to the varying density in the wall-fluid region. The phenomena are found in this region and also observed if the forcing wavelength is of the order of this wall–fluid region, that is, for sufficiently large k_n. To understand the effect of density variation, we again investigate the local shear pressure as this is the fundamental quantity. The momentum balance equation in the steady state, but now for varying density, $\rho = \rho(z)$, reads

$$\rho(z) A \sin(k_n z) = \frac{\mathrm{d}P_{xz}}{\mathrm{d}z}, \tag{27}$$

thus, the actual shear pressure can be obtained simply from integration, i.e.,

$$P_{xz}(z) = A \int_0^z \rho(z') \sin(k_n z')\, \mathrm{d}z' = -\frac{A \cos(k_n z)}{k_n} \rho + \frac{A \sin(k_n z)}{k_n^2} \frac{\mathrm{d}\rho}{\mathrm{d}z} + \cdots - P_{xz}(0) \tag{28}$$

for $k_n \neq 0$. For $k_n = 0$, the shear pressure is 0. Interestingly, shear pressure depends on the product of the driving force and the density derivatives. The series converges very slowly and is not applicable in practice if one needs to use the higher order numerical derivatives of the density.

To proceed, we therefore write the density in terms of its Fourier cosine series,[8,29]

$$\rho_z(z) = \rho_0 + \sum_{i>0} \rho_i \cos(k_i z), \tag{29}$$

where ρ_i is the ith Fourier coefficient corresponding to the wave vector $k_i = 2\pi i/h$. Substitution of this series into Eq. (28) gives upon integration

$$P_{xz}(z) = -\frac{A\rho_0}{k_n}\cos(k_n z) - P^c_{xz}(z), \tag{30}$$

where P^c_{xz} is the shear pressure correction term coming from the density variations,

$$P^c_{xz} = A\sum_{i>0}\frac{\rho_i}{2}\left[\frac{\cos((k_i+k_n)z)}{k_i+k_n} + \frac{\cos((k_i-k_n)z)}{k_n-k_i}\right]. \tag{31}$$

From this, we confirm the expected behavior, namely, that in the limit of zero wave vector the shear pressure follows the constant density local model, $P_{xz} = -A\rho_0/k_n \cos(k_n z)$ since $\lim_{k_n\to 0} P^c_{xz} = 0$. Also, we see that there exists a divergent resonance mode at $k_i = k_n$.

From the momentum balance equation, it is clear that the gradient of the shear pressure is the force density experienced by the fluid. Figure 5 shows the force density contribution from the correction term, P^c_{xz}, normalized with respect to the amplitude predicted by the classical theory, that is, $k_n/(A\rho_0)\,\mathrm{d}P^c_{xz}/\mathrm{d}z$. The inset shows the Fourier coefficients which are independent of the applied forces used here. The effect of density variations on the force in the wall–fluid interface is significant and increases with k_n, that is, the applied force wave vector. For $n = 3$, the correction term in the wall–fluid region is of the same magnitude as the classical prediction amplitude, and the classical theory breaks down. For this wave number, we also observe the velocity profile plateau, point (iii), and this is the reason why we attribute the density variations to be the mechanism behind the plateau. The correction quickly decays as k_n decreases; for $n = 1$ the correction term is only around 10% of the classical prediction. Note, for $n = 1$ the plateau is absent in agreement with the conjecture.

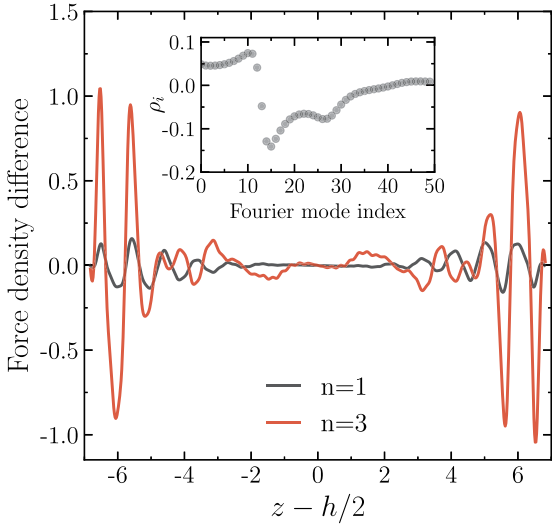

FIG. 5. Force density contribution from the correction term for the shear pressure normalized with respect to the classical prediction amplitude. Black line is for wave number $n = 1$ and red for $n = 3$. Inset shows the Fourier coefficients for the density profile used as input to Eq. (31).

Derivation of the corresponding velocity profile will require a non-local constitutive model as we used above, however, at the wall–fluid boundary we cannot apply the infinite spatial extension and the spatial support of the kernel is unclear; we will not pursue this further. For more on this, the reader is referred to Ref. 30.

It is important to mention that the first attempt to account for the effect of density variations on the flow properties is due to Bitsanis *et al.*[16,31] who proposed the local average density model (LADM). In this approach, the effects of large density variations are dramatically reduced by density averaging. While the LADM has been applied successfully to different flow systems, see, e.g., Ref. 32, it cannot account for the flow enhancement observed here, which is explained by the non-local effects.[5,12,14]

C. Relaxation dynamics

Figure 6 shows the relaxation from the steady state to zero flow for $n = 1$ and (a) $h = 5.74$ and (b) $h = 13.74$. Data are shown as symbols and lines are spline fits to data, which serve as a guide to the eye. For the smaller channel, the relaxation is fast as predicted by the theory, and the velocity shows a small overshoot indicating a visco-elastic response as it was illustrated in Fig. 1.

To reduce the noise-to-signal ratio, we investigate the average relaxation dynamics in a spatial region in the channel. Let z_i and z_{i+1} define the spatial boundaries of a region of interest, then

$$\bar{u}(t) = \frac{1}{\Delta z}\int_{z_i}^{z_{i+1}} u(z,t)\,\mathrm{d}z, \tag{32}$$

such that $\Delta z = z_{i+1} - z_i$ is the region height. For the Newtonian fluid, this gives

$$\bar{u}^N(t) = \frac{A(\cos(k_n z_i) - \cos(k_n z_{i+1}))}{\nu_0 k_n^3 \Delta z}\exp(-\mu t), \tag{33}$$

and for the Maxwellian fluid,

$$\bar{u}^M(t) = \frac{A(\cos(k_n z_i) - \cos(k_n z_{i+1}))}{\nu_0 k_n^3 \Delta z}\exp(-\Gamma t)\Lambda(t). \tag{34}$$

It is natural to let the averaging region be defined by the half-wave of the driving force such that $z_i = ih/(2n)$, $i = 0, 1, \ldots, 2n$, and therefore $\Delta z = h/(2n)$. Due to symmetry, one can further average the velocity in the pair of regions (taking the sign into account) with same distance to the wall, i.e., $i = 0$ and $i = 2n$, $i = 1$ and $i = 2n - 1$, and so forth. The region pairs we symbolize with a natural number and the same number with dagger, for example, 1 and $1^\dagger$ in Fig. 6.

Figure 7 shows the normalized spatial average relaxation dynamics for $n = 1$ and $h = 5.74$, 13.74, 27.74, and 43.73. The spatial average is performed over region 1 and $1^\dagger$ as explained above. For the three largest channel heights, the relaxation data are predicted very well by

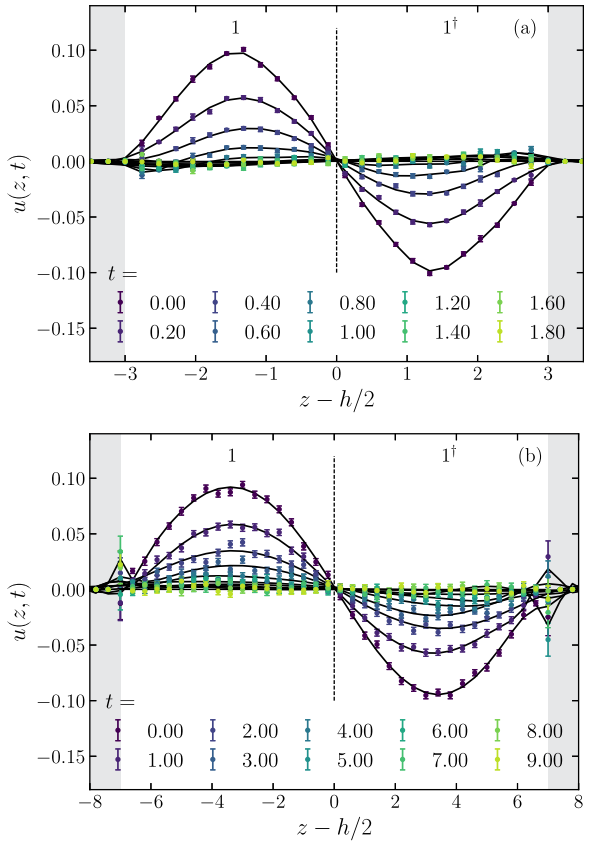

FIG. 6. Snap-shots of the velocity profiles for $n = 1$. In (a) $h = 5.74$ and in (b) $h = 13.74$. Symbols are simulation data and lines are spline fits shown to guide the eye. The vertical dashed line shows the separation of the region intervals used in the spatial averaging, and the numbering refers to the interval. Shaded regions depict the walls.

Newton's law of viscosity, Eq. (33), again without any fitting using $\eta_0 = 1.6$.

For $h = 5.74$, where $\Delta z = 2.87$ and $k_{n=1} = 1.05$ the system features a visco-elastic relaxation; this visco-elastic behavior is consistent with the small length-scale relaxations from thermal perturbations in equilibrium.[5] We fit the data to the Maxwell model, Eq. (34), in two different ways. First, we use the Green–Kubo shear viscosity, $\eta_0 = 1.6$, allowing τ_M to be the only fitting parameter; the result of this gives the full line in Fig. 7 with $\tau_M = 0.14$. It is clear that this yields poor agreement with data. In the second approach, both η_0 and τ_M are fitting parameters (dashed line) giving $\eta_0 = 1.39$ and $\tau_M = 0.20$. The second fitting procedure gives better agreement and results in a lower viscosity, indicating a reduced viscous dissipation on these small length scales; this is in agreement with Ref. 33, where multiscale equilibrium relaxations are studied. It is also interesting to note that the relaxation for $h = 5.74$ appears exponential in accordance with theory at very short times, where the corresponding bulk fluid is in the ballistic regime.

In Fig. 8, relaxation snap-shots for $h = 13.74$ are shown for wave numbers $n = 2$ (a) and $n = 3$ (b). Again, symbols are raw data and lines are spline fits to the data. Recall that for these wave numbers, the

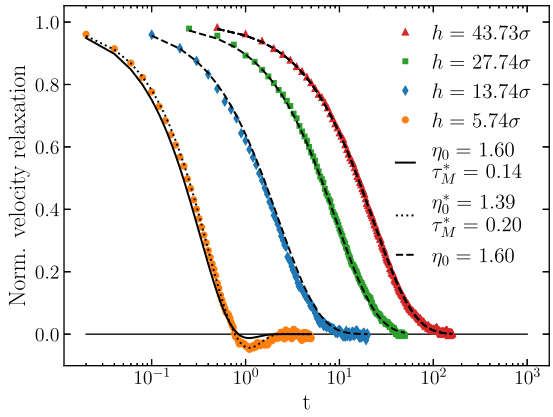

FIG. 7. Normalized averaged velocity relaxation for $n = 1$ and four different channel heights $h = 5.74, 13.74, 27.74$, and 43.73. Symbols are averaged simulation data and lines theoretical predictions, where Eq. (33) is used for $h = 13.74, 27.74, 43.73$ and Eq. (34) for $h = 5.74$. For the three largest channels, no fitting is employed using the Green–Kubo viscosity $\eta_0 = 1.6$. For $h = 5.74$ Eq. (34) is fitted to data using one parameter, τ_M, (full line) and two parameters, τ_M and η_0 (dotted line); see text for further details.

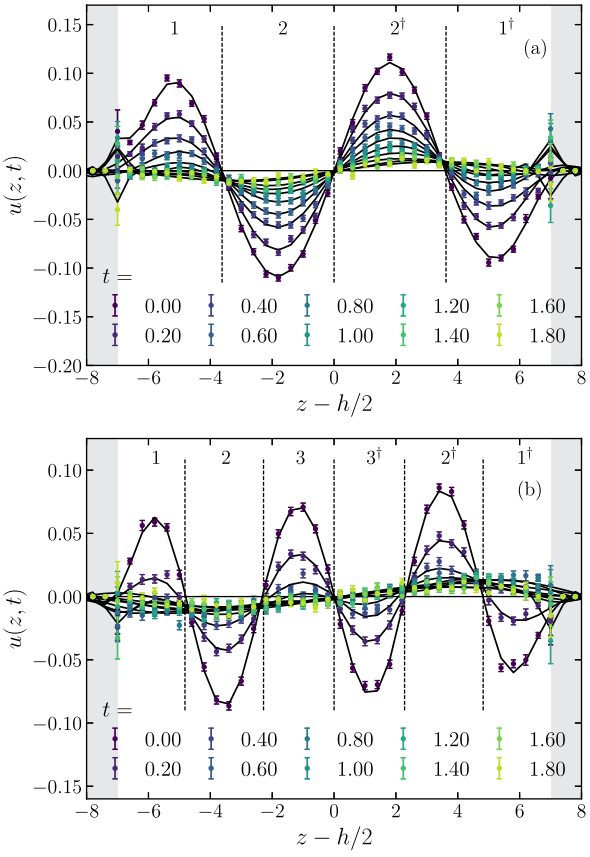

FIG. 8. Snap-shots of the velocity relaxation profiles for $h = 13.74$. In (a) $n = 2$ and in (b) $n = 3$. Symbols are simulation data and lines are spline fits (trend lines). The numbers indicate the region intervals used in the spatial averaging. Shaded regions depict the walls.

steady-state velocity profile is affected by the density gradient in the wall–fluid region as well as non-local viscous response properties. Figure 9(a) plots the corresponding spatial relaxation averages over the regions indicated in Fig. 8. Also, the overall system average relaxation is shown.

For $n = 2, \Delta z = 3.44$, we observe different local relaxation dynamics: The region closest to the wall, regions 1 and $1^\dagger$, are characterized by large densities and density variations, and features clear visco-elastic behavior. The relaxation is fitted to the Maxwell model, Eq. (34), using τ_M as fitting parameter with $\eta_0 = 1.6$. The best fitted Maxwell time is $\tau_M = 0.26$, which is different from the corresponding value found in Fig. 7, $\tau_M = 0.14$, indicating a difference in the relaxation dynamics, and in particular, an enhanced elastic response. The relaxation dynamics around the channel center, regions 2 and $2^\dagger$, is fitted to the Newtonian model using η_0 as a fitting parameter obtaining $\eta_0 = 1.24$, likely due to the non-local effect.

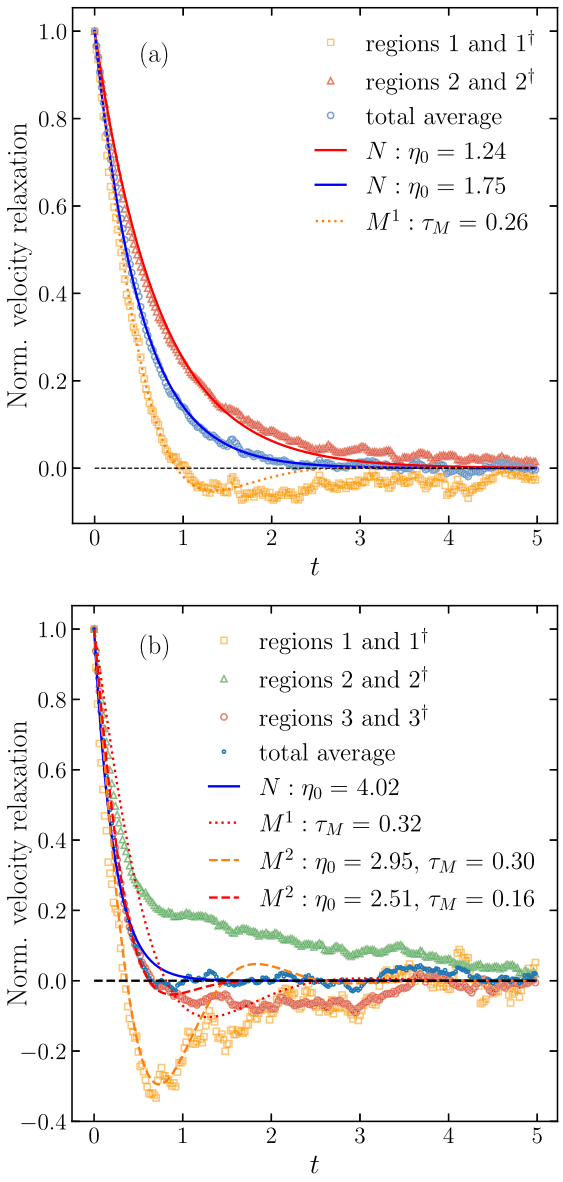

FIG. 9. Normalized averaged velocity relaxation for $h = 13.74$ and (a) $n = 2$ and (b) $n = 3$. Symbols are averaged simulation data and lines the theoretical predictions, Eqs. (33) or Eq. (34), see legends for the parameter values.

The system's overall average relaxation for $n = 2$ is a visco-elastic relaxation. While it does not feature an overshoot, it can appear purely viscous, but, with a higher viscosity coefficient compared to bulk. This apparent increased viscosity can be the mechanism behind the so-called enhanced viscosity reported in the literature, see, e.g., Ref. 34, but we argue here that the "enhancement" is actually an increased elastic response on small length scales even if the overshoot is absent.

The different dynamics in the channel is even more evident for the mode corresponding to $n = 3$, Fig. 9(b), where the half-wavelength is $\Delta z = 2.29$. In the wall–fluid regions, regions 1 and $1^\dagger$, the elastic response is further enhanced as the average is performed over a smaller region where the density layering is more pronounced. For the next half-wave, regions 2 and $2^\dagger$, we observe a surprising relaxation that does not feature any clear viscous or visco-elastic response; initially, the relaxation appears exponential but transitions to a linear decay. Naturally, a fit of Eqs. (33) or (34) to data results in very poor agreement. Thus, the classical description fails in this local region and neither the Newton nor Maxwell model is not applicable. One can, of course, fit an exponential (or Prony) series to the relaxation curves, which will reveal a spectrum of relaxation times, or model the relaxation using more advanced visco-elastic models, like the Maxwell–Weichert element; however, it is the purpose here to test the two standard models. This is an interesting question and warrants a separate, more detailed investigation in future.

It is also interesting that this region features maximum amplitude in the steady state, Fig. 3. In the channel mid-region, the dynamics again changes showing a clear visco-elastic response on the length scale of Δz. As it is the case for $n = 2$, the system overall average relaxation dynamics appears to involve no elastic component even if this is indeed present on the small length scale.

IV. CONCLUSION

We here investigated the nanoscale dense fluid response to a sinusoidal varying driving force for different channel heights and external force wavelengths. It was shown that for sufficiently large driving force wavelengths and channel heights both of the order of 10 particle diameter, the steady-state velocity profile is correctly predicted by classical hydrodynamics using Newton's viscosity law. For small wavelengths, the classical theory breaks down, which we showed to be due to (i) non-local fluid response and (ii) the presence of density variations in the wall–fluid region.

The relaxation from the steady state to zero flow was also studied. Again, the relaxation dynamics is well described by hydrodynamics for large wavelength and channel height. For small channel heights, the Maxwell model correctly captures the visco-elastic overshoot; however, it fails quantitatively and as a consequence both the Maxwell time and the viscosity must be used as free fitting parameters. For small wavelengths, the relaxation dynamics varies with respect to position. As expected, the elastic component is enhanced, and in the wall–fluid interface the density layering greatly affects the local transport properties. In general, we conclude that the wall–fluid interfacial region

features pronounced visco-elastic response compared to the bulk region at the same length scale.

We wish to highlight the region between the wall–fluid interface and the bulk: In the steady state, it features the maximum velocity amplitude over the entire profile, and the relaxation dynamics is very different from the other regions in that it falls into two different regimes, namely, (i) initial exponential relaxation and (ii) what appears to be a linear relaxation. The classical theory cannot even qualitatively account for the dynamics.

It is natural to extend the investigation to even higher wave numbers, however, the underlying modeling applied here will fail in this case, for example, due to the coupling between the strain rate gradient and the density which is not included here, see Refs. 29, 35, and 36. The effects of increasing the wave number will also be enhanced by the complex interfacial dynamics. We expect this to be a focus in future research.

ACKNOWLEDGMENTS

The authors thank Professor Peter Daivis for fruitful comments.

AUTHOR DECLARATIONS

Conflict of Interest

The authors have no conflicts to disclose.

Author Contributions

Solvej Knudsen: Conceptualization (equal); Formal analysis (equal); Investigation (equal); Methodology (equal); Validation (equal); Visualization (equal); Writing – original draft (equal); Writing – review & editing (equal). **B D. Todd:** Conceptualization (equal); Formal analysis (equal); Investigation (equal); Methodology (equal); Supervision (equal); Validation (equal); Visualization (equal); Writing – review & editing (equal). **J. S. Hansen:** Conceptualization (equal); Formal analysis (equal); Investigation (equal); Methodology (equal); Supervision (equal); Validation (equal); Visualization (equal); Writing – original draft (equal); Writing – review & editing (equal).

DATA AVAILABILITY

The data that support the findings of this study are available from the corresponding author upon reasonable request.

APPENDIX A: NEWTONIAN RELAXATION

The momentum balance equation for the geometry shown in Fig. 1 and when no external force is applied is given in Laplace space as

$$\rho(s\hat{u}(z,s) - u_0(z)) = -\frac{\partial}{\partial z}\hat{P}_{xz}(z,s), \tag{A1}$$

where the hat-symbol indicates the Laplace transform, $s = \alpha + i\omega$ is the generalized Laplace coordinate with dimension inverse time, and $u_0(z)$ is the initial condition given in Eq. (5). Using Newton's law of viscosity, Eq. (3), in Laplace space, we have

$$\hat{P}_{xz}(z,s) = -\eta_0 \frac{\partial \hat{u}(z,s)}{\partial z}, \tag{A2}$$

the following second order non-homogeneous differential equation can be obtained:

$$\frac{\partial^2 \hat{u}}{\partial z^2} - \frac{s}{\nu_0}\hat{u} = -\frac{1}{\nu_0}u_0(z). \tag{A3}$$

Here, $\nu_0 = \eta_0/\rho_0$ is the kinematic viscosity. The differential equation is of the general form given by

$$\frac{\partial^2 \hat{u}}{\partial z^2} + a(s)\hat{u} = b, \tag{A4}$$

with

$$a(s) = -\frac{s}{\nu_0} \quad \text{and} \quad b = -\frac{1}{\nu_0}u_0(z). \tag{A5}$$

The general solution is given as the sum of the homogeneous and particular solutions as $u = u_h + u_p$, with

$$u_h = C_1 e^{\xi z} + C_2 e^{-\xi z}, \quad \xi^2 = \frac{s}{\nu_0}. \tag{A6}$$

The no-slip boundary conditions in Laplace space are

$$\hat{u}(0,s) = \hat{u}(h,s) = 0, \tag{A7}$$

from which the coefficients C_1 and C_2 can already be seen to be zero. The solution is thus given by the particular solution $u = u_p$. Guessing the particular solution to be

$$\hat{u}_p(z) = Cu_0(z) \tag{A8}$$

and solving Eq. (A4) for $\hat{u}_p$ gives

$$C = \frac{1}{\mu + s}, \tag{A9}$$

where $\mu = \nu_0 k_n^2$. The specific solution is then given by

$$\hat{u}(z,s) = \frac{1}{\mu + s}u_0(z), \tag{A10}$$

in agreement with the boundary conditions. Performing an inverse Laplace transformation [using $\mathcal{L}^{-1}[1/(s-a)] = \exp(at)$], the solution in time is

$$u(z,t) = u_0(z)e^{-\mu t}. \tag{A11}$$

APPENDIX B: MAXWELLIAN RELAXATION

The Maxwell time τ_M is introduced by Maxwell's model, Eq. (9), as constitutive equation instead of Newton's law of viscosity. In Laplace space, it reads

$$\frac{\partial \hat{u}(z,s)}{\partial z} = -\frac{1}{\eta_0}(1 + \tau_M s)\hat{P}_{xz}(z,s) + \frac{\tau_M}{\eta_0}P_{xz}(z,0), \tag{B1}$$

where the last term is the initial shear pressure for which the external force has been lifted, but the relaxation has not yet started. We can use Newton's law of viscosity to express this in terms of $u_0(z)$ as

$$P_{xz}(z,0) = -\eta_0 \frac{\partial u_0(z)}{\partial z}. \tag{B2}$$

Taking the spatial derivative of Eq. (B1), we get

$$\frac{\partial^2 \hat{u}}{\partial z^2} = -\frac{1}{\eta_0}(1+\tau_M s)\frac{\partial \hat{P}_{xz}}{\partial z} + \frac{\tau_M}{\eta_0}\frac{\partial}{\partial z}P_{xz}(z,0). \tag{B3}$$

Inserting $u_0(z) = A/(\nu_0 k_n^2)\sin(k_n z)$ in Eq. (B2) and taking the derivatives give

$$\frac{\partial}{\partial z}P_{xz}(z,0) = \rho_0 A \sin(k_n z). \tag{B4}$$

Inserting this into Eq. (B3) and isolating $\hat{P}_{xz}$ gives

$$\frac{\partial \hat{P}_{xz}}{\partial z} = -\frac{\eta_0}{1+\tau_M s}\frac{\partial^2 \hat{u}}{\partial z^2} + \frac{\tau_M \rho_0 A}{1+\tau_M s}\sin(k_n z). \tag{B5}$$

Inserting Eq. (B5) and the initial condition $u_0(z)$ into the momentum balance equation Eq. (A1), the equation for $\hat{u}$ is obtained as

$$\frac{\partial^2 \hat{u}}{\partial z^2} - \frac{s(1+\tau_M s)}{\nu_0}\hat{u} = \frac{\tau_M \mu - (1+\tau_M s)}{\nu_0}u_0(z), \tag{B6}$$

where again we use $\mu = \nu_0 k_n^2$. Equation (B6) is on the same general form as in the previous case. The coefficients are

$$a(s) = -\frac{s(1+\tau_M s)}{\nu_0}, \tag{B7}$$

$$b(s) = \frac{\tau_M \mu - (1+\tau_M s)}{\nu_0}u_0(z). \tag{B8}$$

The homogeneous solution is

$$\hat{u}_h^M(z,s) = C_1 e^{\psi z} + C_2 e^{-\psi z}, \tag{B9}$$

but again, from the no-slip boundary conditions, the coefficients C_1 and C_2 are found to be zero. The particular solution is thus our only concern. We guess the solution as

$$\hat{u}(z,s) = B(s)u_0(z). \tag{B10}$$

Inserting into Eq. (B6) determines $B(s)$ to be

$$B(s) = \frac{1+\tau_M(s-\mu)}{s(1+\tau_M s)+\mu}. \tag{B11}$$

It is now possible to perform an inverse Laplace transform of $B(s)$. The poles of $B(s)$ are

$$s_{1,2} = \frac{-\sqrt{1 \pm 4\mu\tau_M} - 1}{2\tau_M}, \tag{B12}$$

and the zero is (where the numerator is zero)

$$s_0 = \frac{\mu\tau_M - 1}{\tau_M}. \tag{B13}$$

Factorizing $B(s)$ gives

$$B(s) = \frac{s - s_0}{(s-s_1)(s-s_2)} \tag{B14}$$

$$= \frac{s}{(s-s_1)(s-s_2)} - \frac{s_0}{(s-s_1)(s-s_2)}. \tag{B15}$$

We apply the following rules of inverse Laplace transform:

$$\mathcal{L}^{-1}\left\{\frac{1}{(s-a)(s-b)}\right\} = \frac{e^{bt} - e^{at}}{b-a}, \tag{B16}$$

$$\mathcal{L}^{-1}\left\{\frac{s}{(s-a)(s-b)}\right\} = \frac{be^{bt} - ae^{at}}{b-a}. \tag{B17}$$

Then, $B(t)$ becomes

$$B(t) = e^{-\Gamma t}\Lambda(t), \tag{B18}$$

where $\Gamma = 1/(2\tau_M)$ is the attenuation coefficient and $\Lambda(t)$ is defined as

$$\Lambda(t) = \frac{(1-2\tau_M\mu)}{\sqrt{1-4\tau_M\mu}}\sinh(\omega_0 t) + \cosh(\omega_0 t) \tag{B19}$$

with the characteristic frequency given by

$$\omega_0 = \frac{\sqrt{1-4\tau_M\mu}}{2\tau_M}. \tag{B20}$$

The temporal evolution is thus an exponential decay weighted by a sum of hyperbolic sine and cosine functions. In the limit where τ_M approaches the $\tau = 1/4\mu$, this reduces to just an exponential decay as

$$\lim_{\tau_M \to 1/4\mu} \Lambda(t) = 1, \tag{B21}$$

whereas in the case were $\tau_M > 1/4\mu$, $\Lambda(t)$ reduces to

$$\Lambda(t) = \frac{1-2\tau_M\mu}{\sqrt{|1-4\tau_M\mu|}}\sin(\omega_0 t) + \cos(\omega_0 t), \tag{B22}$$

giving two distinct dynamical regions depending on the parameters τ_M and μ.

REFERENCES

[1] J. P. Boon and S. Yip, *Molecular Hydrodynamics* (Dover Publication, New York, 1991). ISBN 0486669491.
[2] J. C. T. Eijkel and A. van den Berg, "Nanofluidics: What is it and what can we expect from it?," Microfluid. Nanofluid. **1**, 249–267 (2005).
[3] J. P. Hansen and I. R. McDonald, *Theory of Simple Liquids* (Academic Press, Amsterdam, 2006). ISBN 9780123705358.
[4] L. Bocquet and E. Charlaix, "Nanofluidics, from bulk to interface," Chem. Soc. Rev. **39**, 1073 (2010).
[5] J. S. Hansen, *Nanoscale Hydrodynamics of Simple Systems* (Cambridge University Press, Cambridge, 2022).
[6] L. Bocquet and P. Tabeling, "Physics and technological aspects of nanofluidics," Lab Chip **14**, 3143 (2014).
[7] J. Koplik, J. R. Banavar, and J. F. Willemsen, "Molecular dynamics of fluid flow at solid surfaces," Phys. Fluids **1**, 781–794 (1989).
[8] K. P. Travis, B. D. Todd, and D. J. Evans, "Departure from Navier-Stokes hydrodynamics in confined liquids," Phys. Rev. E **55**, 4288–4295 (1997).
[9] J. S. Hansen, "Where is the hydrodynamic limit?," Mol. Simul. **47**, 1391 (2021).
[10] J. D. Bonthuis, D. Horinek, L. Bocquet, and R. R. Netz, "Electrohydraulic power conversion in planar nanochannels," Phys. Rev. Lett. **103**, 144503 (2009).
[11] F. Bresme, A. Lervik, D. Bedaux, and S. Kjelstrup, "Water polarization under thermal conditions," Phys. Rev. Lett. **101**, 020602 (2008).
[12] B. D. Todd, J. S. Hansen, and P. J. Daivis, "Nonlocal shear stress for homogeneous fluids," Phys. Rev. Lett. **100**, 195901–195904 (2008).
[13] L. Bocquet and J.-L. Barrat, "Hydrodynamic boundary conditions, correlation functions, and Kubo relations for confined fluids," Phys. Rev. E **49**, 3079 (1994).

[14]J. S. Hansen, P. J. Daivis, K. P. Travis, and B. D. Todd, "Parameterization of the nonlocal viscosity kernel for an atomic fluid," Phys. Rev. E **76**, 041121 (2007).
[15]S. Toxvaerd and E. Praestgaard, "Molecular dynamics calculation of the liquid structure up to a solid surface," J. Chem. Phys. **67**, 5291 (1977).
[16]I. Bitsanis, T. K. Vanderlick, M. Tirrell, and H. T. Davis, "A tractable molecular theory of flow in strongly inhomogeneous fluids," J. Chem. Phys. **89**, 3152 (1988).
[17]K. P. Travis and K. E. Gubbins, "Poiseuille flow of Lennard-Jones fluids in narrow slit pores," J. Chem. Phys. **112**, 1984 (2000).
[18]J. A. Thomas and J. H. McGaughey, "Reassessing fast water transport through carbon nanotubes," Nano Lett. **8**, 2788–2793 (2008).
[19]S. De Luca, B. D. Todd, J. S. Hansen, and P. J. Daivis, "Electropumping of water with rotating electric fields," J. Chem. Phys. **138**, 154712 (2013).
[20]B. D. Todd and P. J. Daivis, *Nonequilibrium Molecular Dynamics* (Cambridge University Press, Cambridge, 2017).
[21]J. S. Hansen, P. J. Daivis, and B. D. Todd, "Local linear viscoelasticity of confined fluids," J. Chem. Phys. **126**, 144706 (2007).
[22]N. Phan-Thien, *Understanding Viscoelasticity: An Introduction to Rheology* (Springer Verlag, Berlin, 2002).
[23]J. C. Maxwell, "On the dynamical theory of gases," Philos. Trans. R. Soc. London **157**, 49 (1867).
[24]N. W. Tschoegl, *The Phenomenological Theory of Linear Viscoelastic Behavior* (Springer-Verlag, 1989).
[25]D. Frenkel and B. Smit, *Understanding Molecular Simulation* (Academic Press, London, 1996).
[26]R. J. Sadus, *Molecular Simulation of Fluids: Theory, Algorithms and Object-Orientation* (Elsevier, 1999).
[27]C. Herrero, T. Omori, Y. Yamaguchi, and L. Joly, "Shear force measurement of the hydrodynamic wall position in molecular dynamics," J. Chem. Phys. **151**, 041103 (2019).
[28]B. D. Todd and J. S. Hansen, "Nonlocal viscous transport and the effect on fluid stress," Phys. Rev. E **78**, 051202 (2008).
[29]B. A. Dalton, P. J. Daivis, J. S. Hansen, and B. D. Todd, "Effects of nanoscale density inhomogeneities on shearing fluids," Phys. Rev. E **88**, 052143 (2013).
[30]P. J. Cadusch, B. D. Todd, J. Zhang, and P. J. Daivis, "A non-local hydrodynamic model for the shear viscosity of confined fluids: Analysis of homogeneous kernel," J. Phys. A **41**, 035501 (2008).
[31]I. Bitsanis, J. J. Magda, M. Tirrell, and H. T. Davis, "Molecular dynamics of flow in micropores," J. Chem. Phys. **87**, 1733 (1987).
[32]H. Hoang and G. Galliero, "Shear viscosity of inhomogeneous fluids," J. Chem. Phys. **136**, 124902 (2012).
[33]J. S. Hansen, "A modified and generalized single element Maxwell visco-elastic model," Phys. Rev. E **110**, L023101 (2024).
[34]S. Granick, "Motion and relaxation of confined fluids," Science **253**, 1374 (1991).
[35]B. A. Dalton, K. S. Glavatskiy, and P. J. Daivis, "Nonlocal response functions for predicting shear flow of strongly inhomogeneous fluids. II. Sinusoidally driven shear and multisinusoidal inhomogeneity," Phys. Rev. E **92**, 012108 (2015).
[36]K. S. Glavatskiy, B. A. Dalton, and P. J. Daivis, "Nonlocal response functions for predicting shear flow of strongly inhomogeneous fluids. I. Sinusoidally driven shear and sinusoidally driven inhomogeneity," Phys. Rev. E **91**, 062132 (2015).